

# A Robust Method for Handling Low Density Regions in Hybrid Simulations for Collisionless Plasmas

Takanobu Amano\*, Katsuaki Higashimori, Keisuke Shirakawa

*Department of Earth and Planetary Science, University of Tokyo, Tokyo, 113-0033, Japan*

---

## Abstract

A robust method to handle vacuum and near vacuum regions in hybrid simulations for space and astrophysical plasmas is presented. The conventional hybrid simulation model dealing with kinetic ions and a massless charge-neutralizing electron fluid is known to be susceptible to numerical instability due to divergence of the whistler-mode wave dispersion, as well as division-by-density operation in regions of low density. Consequently, a pure vacuum region is not allowed to exist in the simulation domain unless some ad hoc technique is used. To resolve this difficulty, an alternative way to introduce finite electron inertia effect is proposed. Contrary to the conventional method, the proposed one introduces a correction to the electric field rather than the magnetic field. It is shown that the generalized Ohm's law correctly reduces to Laplace's equation in a vacuum which therefore does not involve any numerical problems. In addition, a variable ion-to-electron mass ratio is introduced to reduce the phase velocity of high frequency whistler waves at low density regions so that the stability condition is always satisfied. It is demonstrated that the proposed model is able to handle near vacuum regions generated as a result of nonlinear self-consistent development of the system, as well as pure vacuum regions set up at the initial condition, without losing the advantages of the standard hybrid code.

*Keywords:* collisionless plasma, kinetic simulation, hybrid simulation

---

## 1. Introduction

Numerical simulations have been an essential tool to investigate complicated nonlinear phenomena occurring in space and astrophysical plasmas. Although the conventional magnetohydrodynamics (MHD) proves itself useful to describe macroscopic plasma dynamics even in the collisionless regime in which the mean free path for Coulomb collisions is comparable to or larger than the system size, it does not necessarily mean that one can completely ignore important kinetic physics. For example, it is well recognized that one must take into account kinetic effect to understand magnetic reconnection, which has been one of the key processes in magnetospheric physics affecting plasma transport, driving global convection, and perhaps triggering substorms. It is now becoming more and more popular to consider that magnetic reconnection plays a key role in astrophysical environments as well. Another example in which kinetic effect is central is the problem of particle acceleration in collisionless shocks. It requires seamless treatment of both microscopic and macroscopic physics because small-scale phenomena primarily determine the acceleration of low energy particles (or "injection"), while the transport of higher energy particles is predominantly governed by characteristics of MHD turbulence. Kinetic numerical simulations that can simultaneously deal with both macroscopic and microscopic dynamics of the collisionless plasma are indeed essential to investigate these important issues. Among those proposed so far, the best numerical technique for this purpose is probably the hybrid simulation, in which ions are treated kinetically whereas electrons are assumed to be a massless charge-neutralizing fluid (Winske et al., 2001; Lipatov, 2002).

---

\*Corresponding author

*Email address:* amano@eps.s.u-tokyo.ac.jp (Takanobu Amano)

The concept of the hybrid simulation is indeed promising in that it enables us to access the ion dynamics, while seemingly less important but more computationally demanding electron physics has been factored out. It has been widely used to study elementary processes such as plasma instabilities, magnetic reconnection, collisionless fast and slow shocks (e.g., Leroy et al., 1982; Winske & Leroy, 1984; Terasawa et al., 1986; Nakamura et al., 1998; Higashimori & Hoshino, 2012). With rapidly increasing computational resources, one may now be able to use a simulation box which is large enough to include the global scale as well. Recently, attempts have been made to model the interaction between the solar wind and relatively small unmagnetized and magnetized solar system bodies by using global hybrid simulations (e.g., Terada et al., 2002; Kallio & Jauhunen, 2003; Trávníček et al., 2007; Holmström et al., 2012; Dyadechkin et al., 2013). On the other hand, it has been well known that hybrid simulations are in practice susceptible to numerical instability. Despite the long history of this technique, to the authors knowledge, any fundamental solutions to this problem has not been given. It is indeed a serious obstacle that hinders application to many important and interesting problems in space and astrophysical plasma physics. The primary purpose of the present paper is to provide a practical solution to the problem of numerical stability in the hybrid simulation. As we will see below, this can be realized by introducing a new way to include finite electron inertia effect.

It is well known that the Alfvén wave at short wavelength comparable to ion inertia length has dispersion due to the decoupling between ion and electron dynamics. There thus appears the whistler mode whose frequency diverges as  $\omega \propto k^2$ . This means that the maximum phase velocity in the system increases rapidly without bound, implying numerical difficulty. This is probably a part of the reasons for the numerical instability in hybrid simulations. It is thus easy to expect that inclusion of finite electron inertia can help stabilizing the simulation because the maximum phase velocity in this case is limited by roughly the electron Alfvén speed. Even with finite electron inertia, however, a numerical problem arises in regions of low density. This is obviously due to the division-by-density operation needed to calculate the electric field from ion moment quantities, which makes it impossible to handle such (near) vacuum regions. In practice, numerical difficulty arises even long before this limit is reached because the Alfvén speed increases as the density decreases, imposing a severe restriction on the simulation time step.

The method we propose in the present paper essentially resolves all these numerical difficulties. Our strategy is also to introduce finite electron inertia effect to limit the maximum phase velocity in the system. We argue that the way in which the electron inertia is introduced is a key to solve the problem. An electron inertia correction term has conventionally been introduced to the magnetic field and its electric field counterpart is often neglected (e.g., Kuznetsova et al., 1998; Shay et al., 1998; Nakamura et al., 2008). By modifying the procedure so that the correction is introduced directly to the electric field, we show that the division-by-density operation is almost eliminated from the simulation procedure. In addition to this, to reduce the maximum wave phase velocity in a low density region, the ion-to-electron mass ratio is considered to be a variable quantity. That is, the mass ratio is reduced locally so that the CFL (Courant-Friedrichs-Lewy) condition is automatically satisfied. We demonstrate that the proposed model implemented in a one-dimensional (1D) hybrid simulation code can successfully follow nonlinear evolution of the system even when extremely low density regions appear as a result of strong instabilities. Furthermore, we also show that the code is able to handle pure vacuum regions, as well as the interface between vacuum and finite density plasma regions. These features suggest that the present model is indeed very robust and will help stabilizing simulations applied to many important problems in space and astrophysical plasmas.

The present paper is organized as follows. First, we present a simulation model in section 2, in which a new way to introduce finite electron inertia is discussed. Numerical implementation is explained in section 3. Section 4 shows simulation results of several test problems. Finally, summary and conclusions are given in section 5.

## 2. Simulation Model

### 2.1. Standard Hybrid Model

For the sake of completeness and to clarify the differences, we first describe the standard hybrid model. Readers who are already familiar with the hybrid model and its assumptions can skip this subsection. Tutorials and comprehensive reviews of the hybrid code are found elsewhere (Winske et al., 2001; Lipatov, 2002).

The basic equations used in the hybrid model are consisting of equation of motion for individual ions and for a fluid electrons

$$\frac{d\mathbf{x}_j}{dt} = \mathbf{v}_j, \quad (1)$$

$$\frac{d\mathbf{v}_j}{dt} = \frac{q_j}{m_j} \left( \mathbf{E} + \frac{\mathbf{v}_j}{c} \times \mathbf{B} \right), \quad (2)$$

$$\frac{d\mathbf{v}_e}{dt} = -\frac{e}{m_e} \left( \mathbf{E} + \frac{\mathbf{v}_e}{c} \times \mathbf{B} \right) - \frac{1}{n_e m_e} \nabla \cdot \mathbf{P}_e, \quad (3)$$

where the subscript  $j$  and  $e$  indicate the indices for individual ions and the electron fluid and other notations are standard.

The electromagnetic fields evolve according to the following Maxwell equations in the Darwin approximation

$$\frac{1}{c} \frac{\partial \mathbf{B}}{\partial t} = -\nabla \times \mathbf{E}, \quad (4)$$

$$\nabla \times \mathbf{B} = \frac{4\pi}{c} \mathbf{J}, \quad (5)$$

and the electric charge density  $\rho$  and current density  $\mathbf{J}$  are defined as

$$\rho = \sum_s q_s n_s - e n_e, \quad (6)$$

$$\mathbf{J} = \sum_s q_s n_s \mathbf{V}_s - e n_e \mathbf{V}_e, \quad (7)$$

where  $q_s, n_s, \mathbf{V}_s$  are the charge, number density and bulk velocity of ion species  $s$  calculated by taking moments of the distribution function. Notice that there is no equation to determine the time evolution of the electric field.

The crucial assumption in the hybrid model is the quasi-neutrality, that is, the electrons move fast enough to cancel any charge-density fluctuations and  $\rho = 0$  is always satisfied. The electron density thus can be written by using ion densities  $n_e \approx n_i \equiv \sum_s q_s n_s / e$ . In addition, the electron bulk velocity may also be eliminated using Ampere's law and the relation  $\mathbf{V}_e = \mathbf{V}_i - \mathbf{J} / n_i e$  where  $\mathbf{V}_i \equiv \sum_s q_s n_s \mathbf{V}_s / n_i e$ . Finally, since the conventional hybrid model ignores the inertia of electron completely ( $m_e \rightarrow 0$ ), one can use the equation of motion for the electron fluid to determine the electric field from given ion moment quantities and the magnetic field. This gives the generalized Ohm's law of the form

$$\begin{aligned} \mathbf{E} &= -\frac{\mathbf{V}_e}{c} \times \mathbf{B} - \frac{1}{n_i e} \nabla \cdot \mathbf{P}_e, \\ &= -\frac{\mathbf{V}_i}{c} \times \mathbf{B} + \frac{1}{4\pi n_i e} (\nabla \times \mathbf{B}) \times \mathbf{B} - \frac{1}{n_i e} \nabla \cdot \mathbf{P}_e. \end{aligned} \quad (8)$$

The second term in the right-hand side is the well-known Hall electric field contribution. Determining the electron pressure tensor by using an appropriate equation of state, the evolution of the system can be followed in time.

## 2.2. Finite Electron Inertia

The conventional way to include a finite electron inertia correction into the hybrid model is to introduce the following so-called generalized electromagnetic field  $\hat{\mathbf{E}}, \hat{\mathbf{B}}$  defined as

$$\hat{\mathbf{E}} = \mathbf{E} - \frac{\partial}{\partial t} \left( \frac{c}{\omega_{pe}^2} \nabla \times \mathbf{B} \right), \quad (9)$$

$$\hat{\mathbf{B}} = \mathbf{B} + \nabla \times \left( \frac{c^2}{\omega_{pe}^2} \nabla \times \mathbf{B} \right), \quad (10)$$

in which the terms proportional to  $\nabla \times \mathbf{B}$  represent electron inertia correction (Lipatov, 2002). It is easy to show that they exactly satisfy Faraday's law:

$$\frac{1}{c} \frac{\partial \hat{\mathbf{B}}}{\partial t} = -\nabla \times \hat{\mathbf{E}}. \quad (11)$$

From the equation of motion for the electron fluid, it may be shown that

$$\hat{\mathbf{E}} = -\frac{\mathbf{V}_e}{c} \times \mathbf{B} - \frac{1}{n_e e} \nabla \cdot \mathbf{P}_e - \frac{m_e}{e} (\mathbf{V}_e \cdot \nabla) \mathbf{V}_e, \quad (12)$$

which is similar to the generalized Ohm's law Eq. (8) but now with the last term which also represents the correction. Note that this equation is not exact; we have dropped the terms  $\partial n_e / \partial t$ ,  $\partial n_i / \partial t$ ,  $\partial n_i \mathbf{V}_i / \partial t$ , assuming ion moment quantities do not change during the fast electron time scale.

Given the generalized electric field  $\hat{\mathbf{E}}$ , one can advance the generalized magnetic field  $\hat{\mathbf{B}}$  by using Eq. (11). The standard electromagnetic field may then be recovered from Eqs. (9) and (10). Further simplifications are commonly adopted; for example, the electric field correction term and electron-scale spatial variation of density are often ignored. In this case, the magnetic field may be recovered by solving the implicit equation

$$\hat{\mathbf{B}} = \left( 1 - \frac{c^2}{\omega_{pe}^2} \nabla^2 \right) \mathbf{B}, \quad (13)$$

and  $\hat{\mathbf{E}} \approx \mathbf{E}$  is assumed. The nice feature with this approach is that the correction can be implemented as a post process to the each integration step of a standard procedure.

Although the above (or similar) set of equations correctly model finite electron inertia effect on transverse modes and have been used for a variety of problems in space physics (e.g., Kuznetsova et al., 1998; Shay et al., 1998; Nakamura et al., 2008), we here prefer to use a different form concerning the numerical stability. Multiplying  $n_e e$  to Eq. (12) and eliminating  $\hat{\mathbf{E}}$  using Eq. (9), one obtains

$$\frac{1}{4\pi} (\omega_{pe}^2 - c^2 \nabla^2) \mathbf{E} = \frac{e}{m_e} \left( \frac{\mathbf{J}_e}{c} \times \mathbf{B} - \nabla \cdot \mathbf{P}_e \right) + (\mathbf{V}_e \cdot \nabla) \mathbf{J}_e, \quad (14)$$

where  $\mathbf{J}_e \equiv -en_e \mathbf{V}_e$  is the electron current density. In deriving this equation,  $\nabla \cdot \mathbf{E} \sim O((V_A/c)^2)$  has been neglected, which is indeed a reasonable assumption. Once the electric field is determined by solving Eq. (14), the magnetic field may be updated using Eq. (4) without invoking the generalized electromagnetic fields.

The present implementation obviously describes the electron scale physics better than the conventional one because it retains the correction term for the electric field as well. Concerning the ions dynamics, however, the effect will be small as it affects only high frequency waves. Nevertheless, the use of Eq. (14) has a remarkable advantage. It is easy to recognize that the terms in the right-hand side of Eq. (14) are proportional to the density. (Or more precisely, they are first and second order moments of the distribution function.) Therefore, in the limit of low density ( $n_e \approx n_i \rightarrow 0$ ), it correctly reduces to the following Laplace's equation:

$$\nabla^2 \mathbf{E} = 0, \quad (15)$$

implying that there is no essential difficulty with this equation in dealing with low density (or vacuum) regions. This is reflected by the fact that the division-by-density operation is "almost" eliminated in the calculation procedure. This will be explained later in more detail.

The idea of solving Laplace's equation instead of the generalized Ohm's law Eq. (8) to obtain the electric field in low density regions is not new. For instance, Harned (1982) used the same idea to allow a vacuum region to exist in a simulation box. In this case, however, the plasma and vacuum regions are essentially distinct and the interface between them must somehow be determined. On the other hand, there is no need to determine such an interface in our case. It is clear from Eq. (14) that these two regions are naturally connected with an intermediate region in between where the electron inertia effect dominates.

Strictly speaking, however, one must recognize the fact that dealing with such a low density region in the hybrid model certainly violates its assumptions. Namely, the quasi-neutrality assumption  $n_e \approx n_i$  is no longer valid in such a tenuous region because time scale associated with the electron plasma oscillation may ultimately become comparable to the simulation time step, and non-negligible charge density fluctuation would appear in reality. It is thus clear that this model does not necessarily give physically correct description of the interface between the plasma and vacuum regions. However, with typical dynamic range of density and grid sizes in hybrid simulations, such a region is not

well resolved anyway. It is thus rather important in practice that a code has capability to handle such regions without numerical problems.

For later use, we rewrite Eq. (14) into the following form

$$\begin{aligned} \left(\rho_e - \frac{m_e c^2}{e} \frac{\nabla^2}{4\pi}\right) \mathbf{E} &= \mathbf{F}(\mathbf{B}, \rho_e, \mathbf{J}_e, \mathbf{P}_e) \\ &\equiv \frac{\mathbf{J}_e}{c} \times \mathbf{B} - \nabla \cdot \mathbf{P}_e + \frac{m_e}{e} (\mathbf{V}_e \cdot \nabla) \mathbf{J}_e + \rho_e \eta \mathbf{J} \end{aligned} \quad (16)$$

where  $\rho_e = en_e (> 0)$  is the electron charge density. Here we have introduced a finite resistivity  $\eta$ . It is easy to see that terms with the  $m_e/e$  factor is due to finite electron inertia which vanishes in the limit  $m_e \rightarrow 0$ , and the standard generalized Ohm's law (8) is recovered.

In Appendix A, a generalized equation for the electric field is derived in a more systematic manner, which reduces to Eq. (14) in a certain limit appropriate for practical purposes.

### 2.3. Electron Pressure

Although so far nothing has been assumed for the electron pressure tensor, in the present study we consider only a scalar pressure  $\mathbf{P}_e = P_e \mathbf{I}$  (where  $\mathbf{I}$  is a unit tensor) determined by the polytropic equation of state for simplicity. To ensure that the pressure becomes zero in a vacuum region  $n_e \approx n_i \rightarrow 0$ , we take  $S \equiv P_e / \rho_e^\gamma$  to be the independent variable where  $\gamma (> 1)$  is the polytropic index for the electron fluid. Since it is a quantity related to the entropy ( $\propto \ln S$ ), its total derivative is zero in the absence of explicit dissipation. In the presence of finite resistivity, we have

$$\frac{d}{dt} S = \frac{\partial}{\partial t} S + (\mathbf{V}_e \cdot \nabla) S = (\gamma - 1) \eta \frac{\mathbf{J}^2}{\rho_e^\gamma}. \quad (17)$$

The electron pressure  $P_e$  may readily be obtained by multiplying  $S$  by  $\rho_e^\gamma$ . It thus vanishes in a vacuum region, consistent with Laplace's equation Eq. (15). Hereafter, the quantity  $S$  is called the electron entropy although it is not so in a strict sense.

Note that the application of our equation for the electric field is not restricted to the specific model of the electron pressure tensor. Extension to any tensor electron pressure models proposed previously, such as those used to study collisionless magnetic reconnection (e.g., Hesse & Winske, 1994; Kuznetsova et al., 1998), is straightforward.

## 3. Numerical Implementation

In this section, implementation of the proposed model to a 1D code is described. We think that the scheme given here is just an example and different methods may also be used and extension to multidimensions should be straightforward because the essential difference from the standard hybrid code is only the way in which the electric field is determined.

### 3.1. Time Integration

The standard Buneman-Boris integration is used to calculate particle trajectories. The particle positions and velocities are defined at the integer and half-integer time steps ( $\mathbf{x}_j^n, \mathbf{v}_j^{n+1/2}$ ), respectively. Accordingly, the electromagnetic field is defined at the integer time step  $\mathbf{E}^n, \mathbf{B}^n$ .

We use the following iterative algorithm of Horowitz et al. (1989) for time integration of the induction equation.

$$\mathbf{B}^{n+1/2} = \mathbf{B}^n - \frac{c\Delta t}{2} \nabla \times \mathbf{E}^{n+1/2} \quad (18)$$

$$\left(\rho_e^{n+1/2} - \frac{m_e c^2}{4\pi e} \nabla^2\right) E_k^{n+1/2} = F_k(\mathbf{B}^{n+1/2}, \rho_e^{n+1/2}, \mathbf{J}_e^{n+1/2}, \mathbf{P}_e^{n+1/2}), \quad (19)$$

$$\rho_e^{n+1/2} E_x^{n+1/2} = F_x(\mathbf{B}^{n+1/2}, \rho_e^{n+1/2}, \mathbf{J}_e^{n+1/2}, \mathbf{P}_e^{n+1/2}), \quad (20)$$

where  $k = y, z$ . Notice that the longitudinal component ( $E_x$ ) does not have the Laplacian correction term. This comes from the fact that the longitudinal and transverse components decouple in 1D, and the correction must operate only

to the transverse component. In multidimensional simulations, one may simply introduce the correction to all the components because (1)  $\nabla \cdot \mathbf{E}$  is small and (2) it is not easy (unless one solves Poisson's equation) to decompose the field into the transverse and longitudinal components.

We define the electron entropy (or equivalently pressure) at the half time step  $S^{n+1/2}$ , which is advanced by using the electron velocity defined at the full time step  $\mathbf{V}_e^n$  as follows

$$S^{n+1/2} = S^{n-1/2} - \Delta t \left[ (\mathbf{V}_e^n \cdot \nabla) S^{n-1/2} + (\gamma - 1) \eta \frac{(\mathbf{J}^n)^2}{(\rho_e^n)^\gamma} \right], \quad (21)$$

and then used to determine the electric field  $\mathbf{E}^{n+1/2}$ . The iteration is typically performed until relative error of the electric field becomes smaller than  $10^{-3}$  at all grid points. Although this formally looks an implicit scheme, we find it is not stable when the CFL condition defined for whistler wave phase velocity is violated.

The electromagnetic field at the next time step is then determined as follows

$$\mathbf{B}^{n+1} = -\mathbf{B}^n + 2\mathbf{B}^{n+1/2} \quad (22)$$

$$\mathbf{E}^{n+1} = -\frac{1}{2}\mathbf{E}^{n-1/2} + \frac{3}{2}\mathbf{E}^{n+1/2}. \quad (23)$$

Notice that the electric field  $\mathbf{E}^{n+1}$  is estimated from those defined at half time steps. We find that naive use of the relation  $\mathbf{E}^{n+1/2} = (\mathbf{E}^{n+1} + \mathbf{E}^n)/2$  results in producing high frequency aliasing noise in the electric field spectrum, which completely vanishes when Eq. (23) is used instead. This may be understood by the fact that the value of  $\mathbf{E}^n$  is not well constrained because adding an arbitrary amount to  $\mathbf{E}^n$  and subtracting the same amount from  $\mathbf{E}^{n+1}$  does not change  $\mathbf{E}^{n+1/2}$ . Since  $\mathbf{E}^{n+1/2}$  is well determined by the above iteration procedure, Eq. (23) better estimates the electric field at the next step.

### 3.2. Spatial Discretization and Electron Inertia Correction

We use the standard staggered mesh for the electromagnetic field  $\mathbf{B}_{i+1/2}$ ,  $\mathbf{E}_i$  with a constant grid spacing  $\Delta x$ . To be consistent with this, ion moment quantities and the electron entropy are defined at the integer grid points:  $\rho_{e,i}$ ,  $\mathbf{J}_{e,i}$ ,  $S_i$ . The second-order central finite difference is used for approximation of spatial derivatives except for the electron entropy equation (21) which is solved by the first-order upwind scheme. It is well known that the staggered mesh can be extended to multidimensions and it guarantees  $\nabla \cdot \mathbf{B} = 0$  within machine epsilon.

We solve the implicit equation (16) for the electric field in an iterative manner. The right-hand-side  $\mathbf{F}$  calculated from the moment quantities and magnetic field at each grid point is used as a source term for solving the equation. The second-order finite difference approximation to the Laplacian operator reduces it to a tridiagonal matrix equation in 1D

$$(-\epsilon E_{k,i-1} + (\rho_{e,i} + 2\epsilon) E_{k,i} - \epsilon E_{k,i+1}) = F_{k,i}, \quad (24)$$

where  $k = y, z$  and  $\epsilon = m_e c^2 / 4\pi e \Delta x^2$ . Notice that  $\epsilon / \rho_e = (c / \omega_{pe} / \Delta x)^2 \lesssim 1$  in practice, meaning that the matrix is diagonally dominant and is relatively easy to invert. In this study, we use the simple symmetric Gauss-Seidel method to solve the matrix equation which is very easy to implement. Although its convergence is known to be slow, experience has shown that only a few iterations are typically sufficient. In general, with higher order discretization and/or in multidimensions, it becomes a band matrix. The diagonally dominant property, however, does not change because it is determined by the fact that the electron inertia is merely a small correction. The situation obviously changes when the grid size is chosen to be small enough to resolve the electron inertia length  $c / \omega_{pe}$  to take into account the electron-scale physics more rigorously. In addition, in the case where a pure vacuum region exists in the simulation domain as is treated in one of the test problems discussed below, the implicit equation essentially reduces to Laplace's equation. In such a case, it is better to use a more sophisticated iterative matrix solver for faster convergence.

It is worth noting that, once the source term is given, the division-by-density operation is not anymore needed to invert the matrix, because the diagonal coefficients (whose inverses are needed) of the matrix is  $\rho_{e,i} + 2\epsilon$ , rather than  $\rho_{e,i}$ . However, we must mention that the calculation of  $\mathbf{V}_e = \mathbf{J}_e / \rho_e$  cannot completely be avoided from the numerical procedure: It appears at the third term of the source term of Eq. (16) and the equation for the electron entropy Eq. (17). Nevertheless, these terms do not pose a serious numerical problem in practice because they represent the Doppler shift

of the waves into the electron-fluid rest frame whenever it is well-defined, while on the other hand, in a vacuum region obviously it cannot be defined. For the present purpose, we redefine the electron velocity as

$$\mathbf{V}_e = \frac{\mathbf{J}_e}{\max(\rho_e, \rho_{e,min})}, \quad (25)$$

where the minimum density  $\rho_{e,min}$  is chosen to correspond to the one-count level in the present study. This makes sure that the electron velocity does not diverge in a vacuum region whereas the modification does not affect results in a cell containing more than one particle. We find this simple fix, combined with the variable mass ratio technique as explained below, is sufficient to keep track of the simulation without numerical problems even for highly nonlinear problems in which near vacuum regions appear in an unexpected manner.

### 3.3. Variable Mass Ratio

The numerical schemes described so far have been shown to be successful when the time step is sufficiently small. However, it may become unstable in highly nonlinear problems in which regions of extremely low density appear as a result of self-consistent time evolution and consequently the maximum phase velocity of the system violates the CFL condition. A much smaller time step is therefore needed for stability, but it is often impractical. We simply try to stabilize the simulation by numerical means at the expense of correct physics whenever they appear in the simulation box.

For a cold plasma, the maximum wave phase velocity in the system is determined from the whistler mode dispersion relation as

$$v_{p,max} \simeq \frac{1}{2} \frac{B}{\sqrt{4\pi n_e m_e}} = \frac{1}{2} V_{A,e} \quad (26)$$

where  $V_{A,e}$  is the electron Alfvén velocity. This upper bound on the phase velocity does not exist in the limit  $m_e \rightarrow 0$  because the electron Alfvén velocity is proportional to  $\sqrt{m_i/m_e}$ .

In general, numerical stability for an explicit scheme at least requires the Courant number defined with respect to the maximum phase velocity to be less than unity:  $v_{p,max}\Delta t/\Delta x \leq 1$ . The phase velocity must therefore be numerically reduced for stability in low density regions. Our strategy here is to consider the mass ratio as a variable quantity. By locally and temporarily modifying the mass ratio, the maximum phase velocity can be reduced so that the CFL condition is always satisfied. More specifically, one may use a modified electron mass  $m'_e$  defined as

$$\frac{m'_e}{m_i} = \max\left(\frac{m_e}{m_i}, V_A^2 \left(\frac{\Delta t}{2\alpha\Delta x}\right)^2\right) \quad (27)$$

instead of the physical electron mass  $m_e$ . Here  $V_A = B/\sqrt{4\pi n_i m_i}$  is the Alfvén speed calculated by using the local density and magnetic field, and  $\alpha$  is the maximum allowed Courant number. In the present paper, we always choose  $\alpha = 1/2$  for safety.

It is important to mention that although this modifies the dispersion relation of whistler waves, low frequency Alfvén waves are not affected as far as  $m_e/m_i \ll 1$  is satisfied. In contrast, if one imposes a floor value in density to reduce the phase velocity, it is modified even in the MHD limit. In addition, since the phase velocity diverges at short wavelength in the limit  $m_e \rightarrow 0$ , the floor value must be chosen much larger than the case with finite electron inertia. It must be pointed out that the electron inertia length  $c/\omega_{pe}$  introduced in hybrid and Hall-MHD models is usually treated as if it were a constant even when the density may change substantially (Kuznetsova et al., 1998; Shay et al., 1998; Nakamura et al., 2008). This corresponds to changing the mass ratio to compensate the density variations. Our treatment is similar, but much better than this because it may change only in the limited region and time in which the stability condition is no longer satisfied. In any case, modification of the finite electron mass will not influence the simulation results as far as the electron inertia scale is not appropriately resolved.

We emphasize that when one is primarily interested in the ion dynamics, a finite electron mass may be seen as an artificial parameter for numerical stability rather than physical, which does not affect the simulation results by assumption. This will hold in most of situations where the hybrid simulation applies and the electron inertia effect is not expected to be important. Otherwise, one must employ a more fundamental model taking into account rigorous electron-scale physics. In Appendix B, validity range of such variable mass ratio technique is discussed.

## 4. Test Problems

In this section, we discuss simulation results for several test problems that demonstrate the robustness of our new method. In the present paper, we fix the number of iteration for the electron inertia correction (symmetric Gauss-Seidel iteration) to 2, while the iteration to determine the electric field (i.e., the Horowitz iteration loop) continues until the relative error of electric fields becomes less than  $10^{-3}$ . Note that we have confirmed that the number of iteration for the electron inertia correction does not change the result significantly.

In the following, unless otherwise stated, time and space are respectively normalized to the inverse ion cyclotron frequency  $1/\Omega_{ci}$  and the ion inertia length  $V_A/\Omega_{ci}$  defined for the average density and magnetic field. The speed of light is held fixed to  $V_A/c = 10^{-4}$  in all the simulation runs presented below. The resistivity is assumed to be zero except for examples shown in section 4.4. The number of grids, number of particle per cell are denoted by  $N_x$ ,  $N_{ppc}$ , respectively. The periodic boundary condition is always used, and the velocity distribution is initialized by isotropic Maxwellian with a given temperature.

### 4.1. Linear Dispersion Relation

We have tested whether our newly developed code can reproduce theoretical linear dispersion relation for a homogeneous plasma with finite electron inertia effect. The simulations are performed without any explicit perturbations and the system evolves solely from thermal noise. The code is verified with various grid spacings and time steps, number of particles per cell, as well as physical parameters such as mass ratio, plasma beta, etc. One of the examples is shown in Fig. 1, which displays the  $\omega-k$  diagram of the transverse electric field obtained with a mass ratio  $m_i/m_e = 100$ , temperature ratio  $T_i/T_e = 1$ , and plasma beta  $\beta_i = 10^{-2}$ . Here, the constant background magnetic field  $B_0$  is imposed along the  $x$  direction and the electric field is normalized to  $V_A B_0/c$  accordingly. Other simulation parameters are as follows:  $\Delta t = 5 \times 10^{-3}$ ,  $\Delta x = 0.1$ ,  $N_x = 256$ ,  $N_{ppc} = 64$ . In this plot, the positive (negative) frequency represents right-hand (left-hand) circularly polarized mode, and similarly signs of the wavenumber indicate different helicities. We see that the agreement between the simulation result and theoretical dispersion relation shown with the solid lines is very good. Notice that, in this figure, the effect of electron inertia appears at  $k\lambda_i \gtrsim 3$ , beyond which the phase velocity is reduced relative to the Hall-MHD dispersion relation shown in the dashed line. We have confirmed that the total energy is in general very well conserved. In this particular run, the error is less than  $\sim 2 \times 10^{-3}$  %.

### 4.2. Electromagnetic Ion Beam Instability

In this section, we discuss simulation results for the resonant electromagnetic ion beam instability which is one of the standard test problems for a conventional hybrid code. The purpose of this test is to show that the present method does not introduce any additional numerical difficulties when applied to problems that can be treated by the standard hybrid model.

The simulation setup is very similar to Winske & Leroy (1984). We choose the relative beam density  $n_b/n_0 = 0.02$ , and bulk velocity  $V_b/V_A = 10$  streaming parallel to the ambient magnetic field, the plasma beta for core ions  $\beta_c = 1.0$ , beam ions  $\beta_b = 1.0$ , and electrons  $\beta_e = 0.1$ . The ion to electron mass ratio is chosen to be  $m_i/m_e = 100$ . In this case, it is easy to find from linear analysis that right-hand circularly polarized electromagnetic waves propagating parallel to the magnetic field are unstable due to cyclotron resonant interaction with the beam ions. The initial magnetic field is thus taken to be along the  $x$  direction. Fig. 2 displays the time evolution of the mode amplitudes that are expected to grow due to this instability. In this simulation, we use  $\Delta t = 0.01$ ,  $\Delta x = 0.25$ ,  $N_x = 1024$ ,  $N_{ppc} = 64$ . It is clear that the simulation results agree very well with the linear theory whose growth rates are shown in dashed lines. Fig. 3 shows a snapshot of the magnetic field, and the ion phase space diagram for both beam and core components just before the saturation. The transverse velocities of beam ions are strongly affected by the excited large-amplitude wave whereas the core ions are modulated only slightly. This feature is consistent with the fact that the instability is excited by the resonance between the wave and beam ions. Fig. 4 shows time evolution of parallel and perpendicular energies for both beam and core ions, as well as the magnetic field energy. One can see that the beam parallel energy is substantially reduced as a result of the instability and transferred to the perpendicular energy of the beam and core components through pitch-angle scattering.

The above linear and nonlinear development of the instability is consistent with previous studies, and thus confirms that the new model can reproduce the standard hybrid simulation results. Note that, in this simulation, the grid size is always much larger than the electron inertia length during the whole run and the electron inertia effect is an



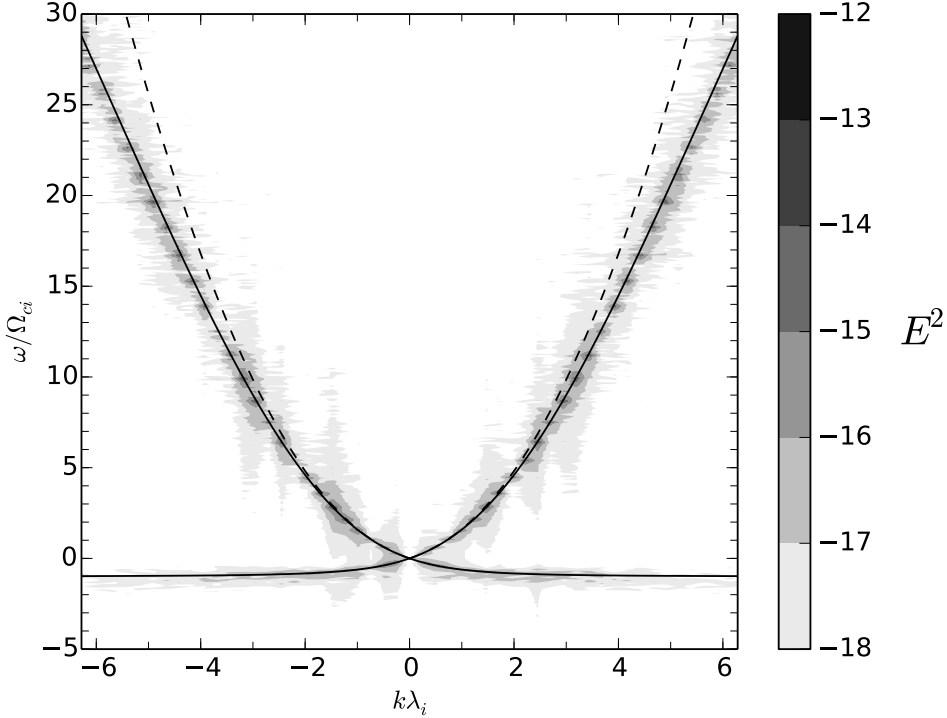


Figure 1: Power spectral density (gray scale) obtained from the simulation for a homogeneous plasma. No explicit perturbations are added at the initial condition. The solid line represents the dispersion relations of circularly polarized electromagnetic waves calculated for a cold plasma. The dashed line shows the dispersion relation corresponding to the Hall-MHD ( $m_e \rightarrow 0$ ).

unimportant small correction. Indeed, the result without the correction appears almost exactly the same. It is important to mention that the inclusion of the electron inertia effect does not impose any numerical difficulties in application of our method to problems where the electron inertia does not play a role.

#### 4.3. Decay Instability

Now we consider an example in which near vacuum (or extremely low density) regions appear as a result of nonlinear and self-consistent development of the system. The standard hybrid method will not be able to keep track of such a simulation owing to its limit on handling low density regions. In contrast, we demonstrate that the present model is free from such difficulty.

To show this, we choose a parametric instability of a large-amplitude circularly polarized Alfvén wave (Goldstein, 1978; Wong & Goldstein, 1986; Terasawa et al., 1986). Although the Alfvén wave is an exact solution of MHD equations even for finite amplitude, it is known to be unstable against perturbations and will decay through the excitation of other waves (daughter waves). Specifically, the decay instability is a process occurring in a low beta plasma that excites a forward-propagating ion-acoustic wave and a backward-propagating Alfvén wave. The simulation parameters are chosen as follows. The parent large-amplitude wave is on the R-mode Alfvén /whistler branch propagating along the ambient magnetic field (taken along the  $x$  direction) with frequency and wavenumber of  $(\omega_0, k_0) = (0.215, 0.196)$  and the amplitude is  $B_p/B_0 = 0.5$  (i.e., 50% of the background magnetic field). The plasma beta (for both ions and electrons) and ion-to-electron mass ratio are  $\beta_i = \beta_e = 10^{-2}$  and  $m_i/m_e = 100$ , respectively. Other parameters are  $\Delta t = 0.01$ ,  $\Delta x = 0.5$ ,  $N_x = 512$ ,  $N_{ppc} = 64$ .

Time evolution of the decay instability is summarized in Fig. 5. In this figure, the transverse magnetic field  $B_y$  is decomposed into different helicities (denoted as  $B_y^+$  and  $B_y^-$ ), and are shown in the left and center panels, respectively. Note that the  $B_y^+$  ( $B_y^-$ ) component includes R-mode (L-mode) waves propagating to the right and L-mode (R-mode)

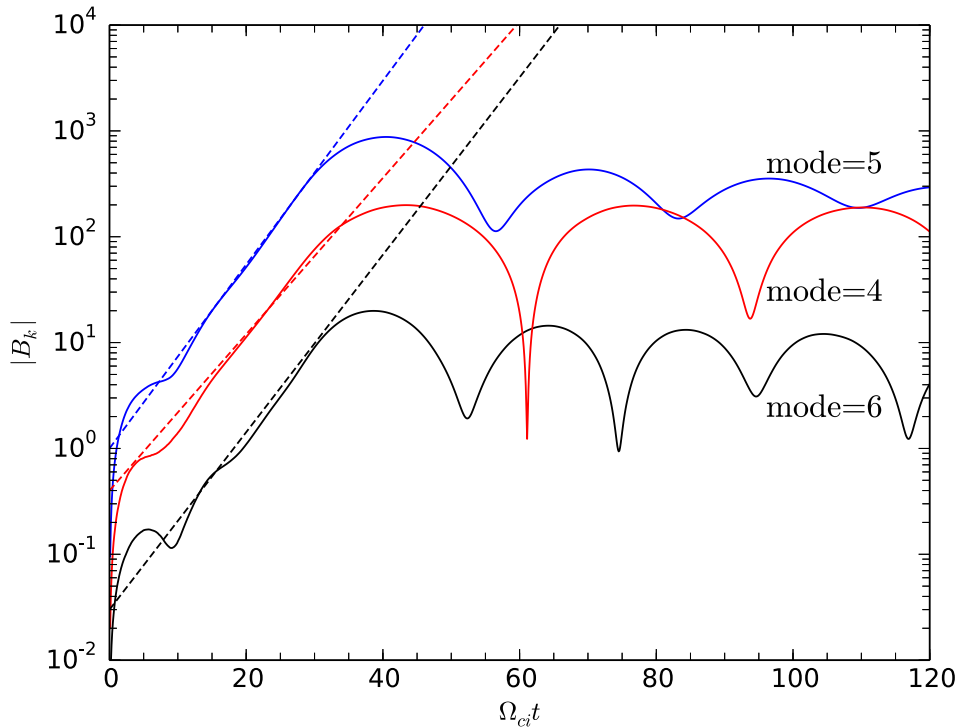


Figure 2: Time evolution of mode amplitudes expected to grow due to the electromagnetic ion beam instability. The different colors represent different modes (mode numbers 4, 5, 6). The dashed lines indicate theoretical linear growth rates for corresponding modes shown in the solid lines.

wave propagating to the left. (See Terasawa et al. (1986) for technical details.) The density fluctuations are also shown in the right panel. The parent wave is a R-mode wave propagating in the positive  $x$  direction with a mode number of 8, which can be easily identified in the left panel at the initial stage. The growth of the instability is seen as the development of large-amplitude density fluctuations. A backward-propagating Alfvén wave is then excited associated with this. For this particular run, the amplitude of density fluctuations is found to be substantial ( $N_i/N_{i,0} \gtrsim 1$ ) at the saturation stage.

Fig. 6 displays the snapshot of density and ion phase space diagram around the saturation  $\Omega_{ci}t = 92.0$ . One can see that clear ion phase-space holes are formed due to the trapping of ions by an electrostatic potential produced by large-amplitude ion-acoustic waves as was found by earlier studies (Terasawa et al., 1986). The large-amplitude density fluctuations are associated with the trapped ion dynamics. The minimum density (during the whole run) goes down to  $\sim 10^{-2}$  relative to the initial density, which is comparable to the one-count level ( $1/N_{ppc} \sim 0.016$ ) for the simulation parameters. Thanks to the new method to determine the electric field as well as the variable mass ratio technique, the appearance of such extremely low density regions does not lead to collapse of the simulation. Note that we have confirmed that a fixed mass ratio makes simulations numerically unstable even if the same equation is used to determine the electric field. Furthermore, even densities below the one-count level do not lead to any numerical problems. Indeed, a simulation with a lower beta ( $\beta = 10^{-3}$ ) with all other parameters fixed is also successful, in which the minimum density becomes as low as  $\sim 10^{-3}$ , i.e., well below the one-count level. This demonstrates the robustness of our model in handling low density (or near vacuum) regions which may appear in an unexpected manner due to nonlinear development of the system. This is a clear advantage over the standard hybrid code.

#### 4.4. Plasma Expansion to Vacuum

Finally, we demonstrate that the present model is able to handle a pure vacuum as well as the interface between plasma and vacuum regions in a seamless manner. One of the examples of such situations occurring in space is

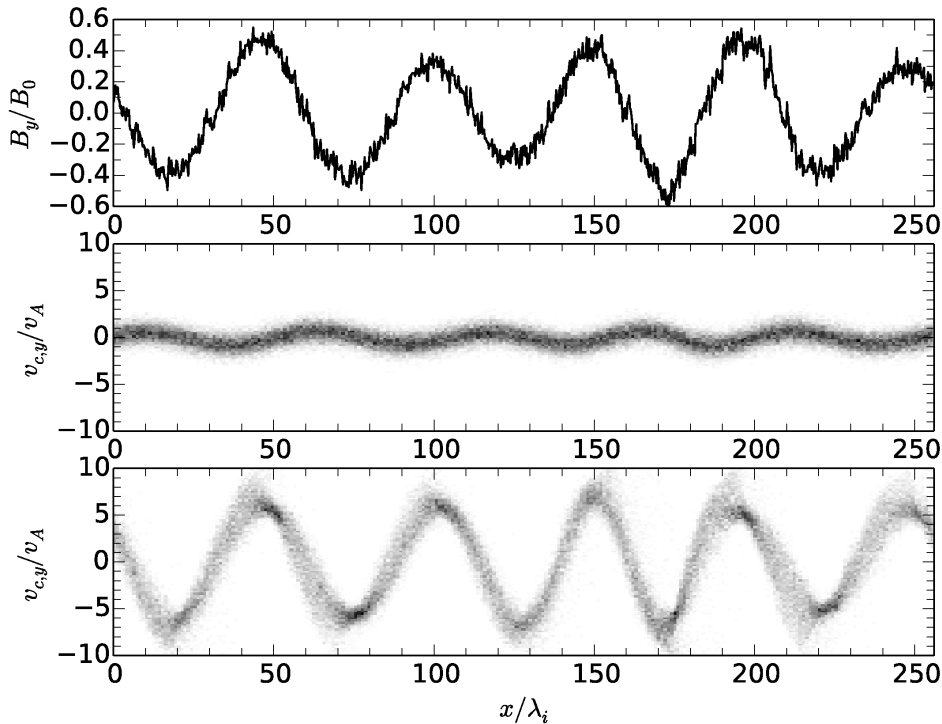


Figure 3: Snapshot of magnetic field  $B_y$  (top) and transverse ion phase space diagram for core (middle) and beam (bottom) components just before the saturation.

the interaction between the solar wind and the Moon (e.g., Holmström et al., 2012). Since the solar wind plasma is obscured, the plasma density is substantially depleted behind the obstacle and a wake region appears which is essentially a vacuum region. The solar wind plasma gradually intrude into the wake owing to a finite thermal velocity and the region will be filled with the plasma again far downstream of the obstacle. Assuming steady state, this refilling process of the wake may be approximately modeled by 1D expansion of a plasma into a pure vacuum region (Farrell et al., 1998; Birch & Chapman, 2001), which is simulated here.

Initially, the system is divided into two regions: the left and right regions respectively correspond to the plasma and vacuum regions. The plasma then freely expands into the vacuum region with their thermal velocity. This can be clearly seen in Fig. 7 showing a snapshot of a typical simulation. The plasma region is initially uniform and is characterized by  $\beta_i = \beta_e = 10^{-2}$ , and  $m_i/m_e = 100$ . The uniform magnetic field  $B_0$  parallel to the  $x$  direction is imposed. Other parameters  $\Delta t = 0.01$ ,  $\Delta x = 0.5$ ,  $N_x = 512$  and  $N_{ppc} = 128$  for the plasma region are used. Note that, in this section, the inertia length and Alfvén velocity (i.e., normalizations) are defined with the average density over the entire simulation box.

Since the magnetic field is along  $x$  direction, particles in the left-hand side of the box with positive velocity can freely propagate to the vacuum region. This free streaming signature can be seen in the ion phase space diagram. In addition, the longitudinal electric field  $E_x$  in the interface region is slightly positive due to the pressure gradient ( $x \sim 130-140$ ), and the ions at the leading edge are accelerated toward the vacuum, a feature consistent with previous particle-in-cell simulations (Farrell et al., 1998; Birch & Chapman, 2001). We see that the code can keep track of the evolution without any numerical instabilities even in the presence of a pure vacuum region. No ad hoc technique is needed in handling the interface region.

There is concern about handling vacuum regions with hybrid codes because a finite current density may numerically arise even in the absence of current carriers. This is because the total current is calculated from the magnetic field and is nothing to do with the plasma density. This clearly contradicts with the basic assumption of the hybrid

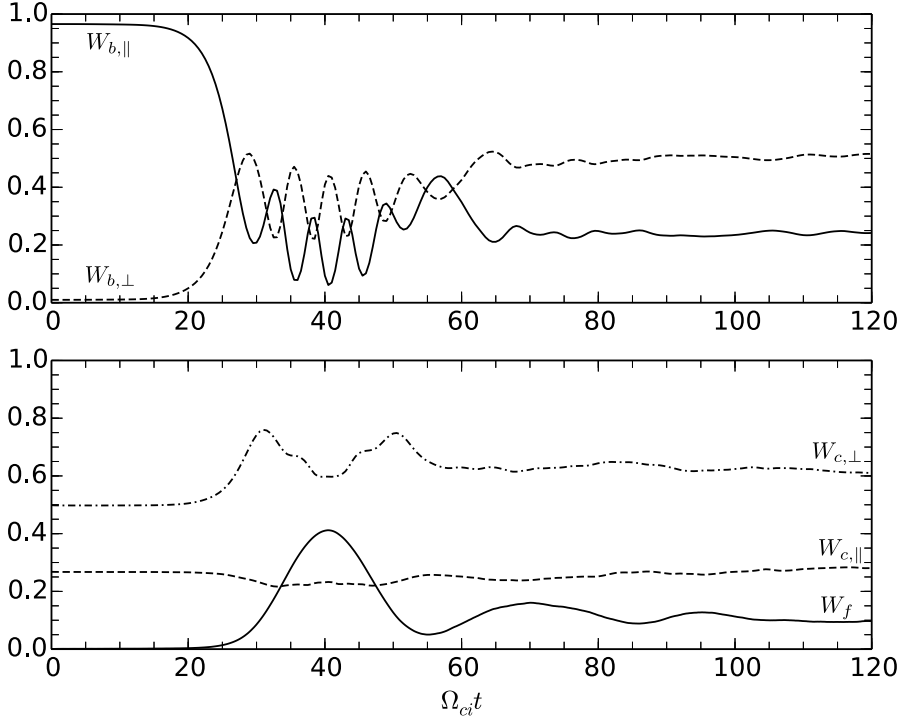


Figure 4: Time history for parallel and perpendicular particle energies for the beam  $W_{b,||}$ ,  $W_{b,\perp}$  (top), core ions  $W_{c,||}$ ,  $W_{c,\perp}$ , and the magnetic field energy  $W_f$  (bottom).

model. To let the system quickly relaxes to a state consistent with the assumption, previous studies have introduced a large resistivity in low density regions (Hewett, 1980; Holmström, 2013). The resulting equation for the magnetic field is a diffusion equation with its coefficient proportional to the resistivity, and the steady state solution is given by a potential magnetic field  $\nabla^2 \mathbf{B} = 0$ . The problem with this approach is that the large resistivity imposes a severe restriction on the time step for an explicit time integration scheme. In contrast to this, our method can better handle this issue.

In the region of our interest, the plasma density  $\rho_e$  approaches to zero, whereas we need a large resistivity  $\eta$ . We may thus assume that  $\eta\rho_e$  remains finite. Then for a sufficiently low density region, the equation for the electric field is reduced to

$$\nabla^2 \mathbf{E} = -\frac{\omega_{pe}^2}{c^2} \eta \mathbf{J}. \quad (28)$$

In this case, by taking rotation of the induction equation, one sees

$$\frac{\partial}{\partial t} (\nabla \times \mathbf{B}) = -\eta \frac{\omega_{pe}^2}{4\pi} (\nabla \times \mathbf{B}) \quad (29)$$

which means that the total current in such a region decays exponentially with a damping rate of  $\eta\omega_{pe}^2/4\pi$ . This equation is clearly a pure damping equation requiring only local information. Therefore, the numerical stability criterion is very much relaxed as compared to the diffusion equation which involves spatial derivatives. Practically, one can use a large resistivity such that the decay time becomes on the order of the simulation time step. Since the total current vanishes as a result, the final state will be given by a potential magnetic field that is equivalent to the diffusion equation approach. Namely, even if a non-zero current density develops for whatever reason, one can enforce it to decay very rapidly

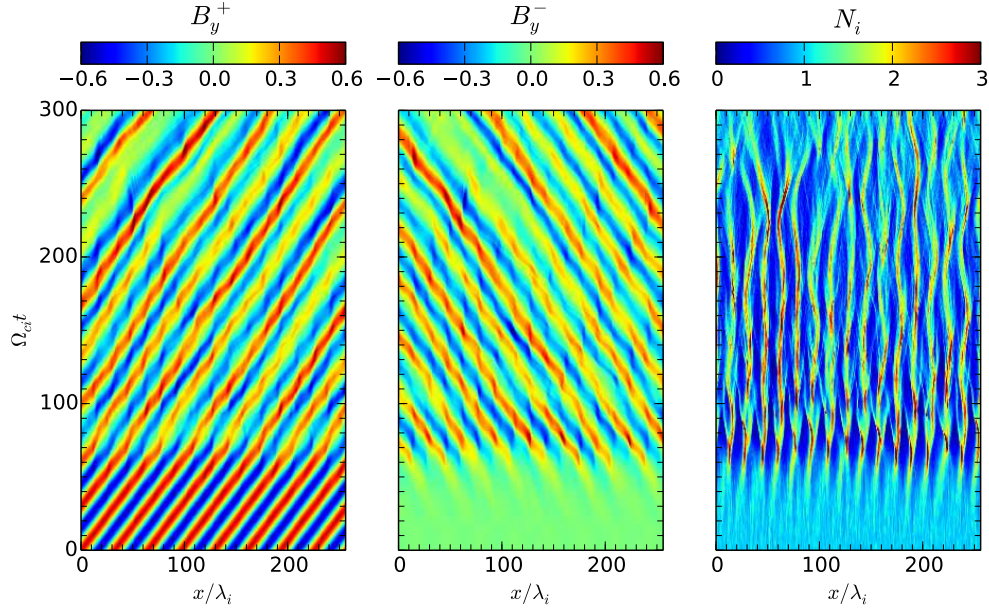


Figure 5: Time evolution of decay instability of Alfvén wave. The left and center panels show  $B_y^+$  and  $B_y^-$  which are calculated using Fourier decomposition of the raw  $B_y$  into different helicities. The right panel shows density fluctuations normalized to the initial uniform density.

within a few time steps by appropriately choosing the resistivity. We have implemented this damping by setting the resistivity as follows:

$$\eta\rho_e = \frac{1}{2} \left( \gamma_{max} \frac{m_e}{e} - \eta_0\rho_e \right) \left( 1 - \tanh \left( \frac{\rho_e - \rho_{min}}{\sigma} \right) \right) + \eta_0\rho_e, \quad (30)$$

where  $\eta_0$  is the background uniform resistivity (chosen to be zero in this study),  $\gamma_{max}$  is the damping rate in vacuum,  $\rho_{min}$  is density corresponding to one particle per cell and we choose  $\sigma = \rho_{min}/2$ . This form of resistivity smoothly connects from the uniform background in the plasma region to the vacuum where the damping rate is chosen to be  $\gamma_{max} = 1/\Delta t$ , and ensures that the large resistive damping operates only in near and pure vacuum regions where  $\rho_e \lesssim \rho_{min}$ .

We have tested the effectiveness of this method by initially setting up non-zero current density by hand in a vacuum region, which shows monotonic and rapid decay of the initial current density as expected (not shown). Results of another nontrivial example are shown in Figures 8 and 9. The setup of this simulation is the same as the previous one except that a localized Alfvénic wave packet propagating in the positive  $x$  direction initially exists in the plasma region. The thickness of Gaussian envelope of the packet is 10 with a wave number of  $k_0 = 0.196$ . The maximum amplitude of the wave packet is 20% of the background field and is therefore large enough for nonlinear effects being visible. Time evolution of  $B_y$  and density is shown in Fig. 8. The wave packet initially propagates to the right and is then reflected off the interface. During its interaction with the interface, the density hump has formed due to a ponderomotive force exerted by the wave packet as seen in the left panel of Fig. 8. This is clearly a nonlinear effect and cannot be seen in smaller amplitude cases, which demonstrates that the present method is robust and stable even in the presence of nonlinear perturbations. A snapshot of the transverse magnetic field  $B_y$ ,  $B_z$  and density and phase space diagram for ions at  $\Omega_{ci}t = 140.0$  are shown in Fig. 9. The wave packet is already reflected at this time and is propagating to the left. In the vacuum region, there exists a small but finite transverse magnetic fields. The magnetic field in vacuum is, however, constant or current-free due to the imposed damping. Although the relaxation time to the assumed state is finite, we think it is practically fast enough, and the relative simplicity is an advantage of our approach.

Note that the simulation can run without introducing resistivity in this particular case, although it gives short wavelength noise both in the plasma and vacuum regions generated during the interaction between the wave packet

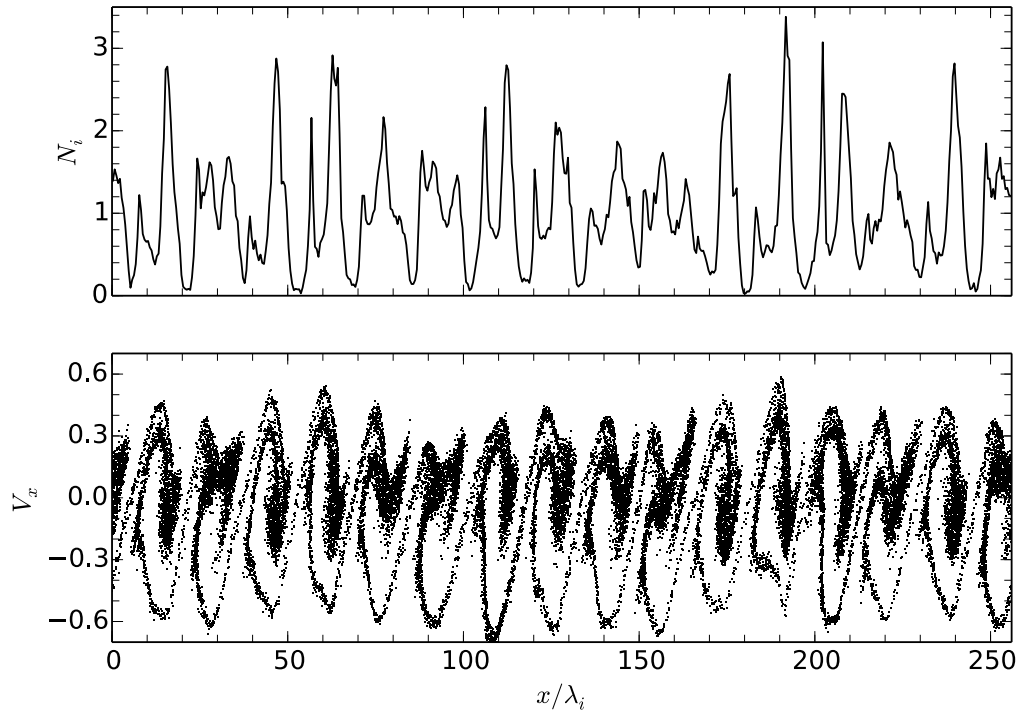


Figure 6: Snapshot of density (top) and ion phase space diagram (bottom) for decay instability of Alfvén wave around the saturation  $\Omega_{ci}t = 92.0$ .

and the interface. Thus, the “vacuum resistivity” is not strictly necessary, but is probably better to be included for numerical stability.

## 5. Summary and Conclusions

In the present paper, we have introduced a new equation to determine the electric field for the hybrid simulations for collisionless plasmas. The equation takes into account finite electron inertia effect and reduces to Laplace’s equation in the limit of low density. This is in clear contrast to the methods proposed so far that consider a correction only to the magnetic field. This difference resolves the fundamental difficulty inherent in the conventional hybrid simulation model, i.e, the impossibility of handling vacuum regions due to the existence of the division-by-density operation in the simulation procedure.

The present method improves numerical stability even for a region of finite density. This is because the inclusion of finite electron inertia imposes a limit of the maximum phase velocity of the system. In addition, it is sometimes needed for numerical stability to introduce a variable mass ratio technique, which ensures the stability by reducing the ion-to-electron mass ratio in regions where the maximum wave phase velocity violates the CFL stability condition. One may think that the electron inertia effect is merely a numerical stabilization factor rather than physics. This will hold in most of situations where the hybrid simulation applies and the electron inertia effect is not expected to be important, or not of primary interest. The proposed method will thus be useful for application of the hybrid code to problems where scale length comparable or longer than ion inertia length is essential, while appearance of low density regions as a result of self-consistent evolution of the system is unavoidable. It is worth mentioning that the method does not deteriorate the advantages of the standard hybrid code. In addition, we think that most of discussion presented in this paper will also apply to the Hall-MHD code as well.

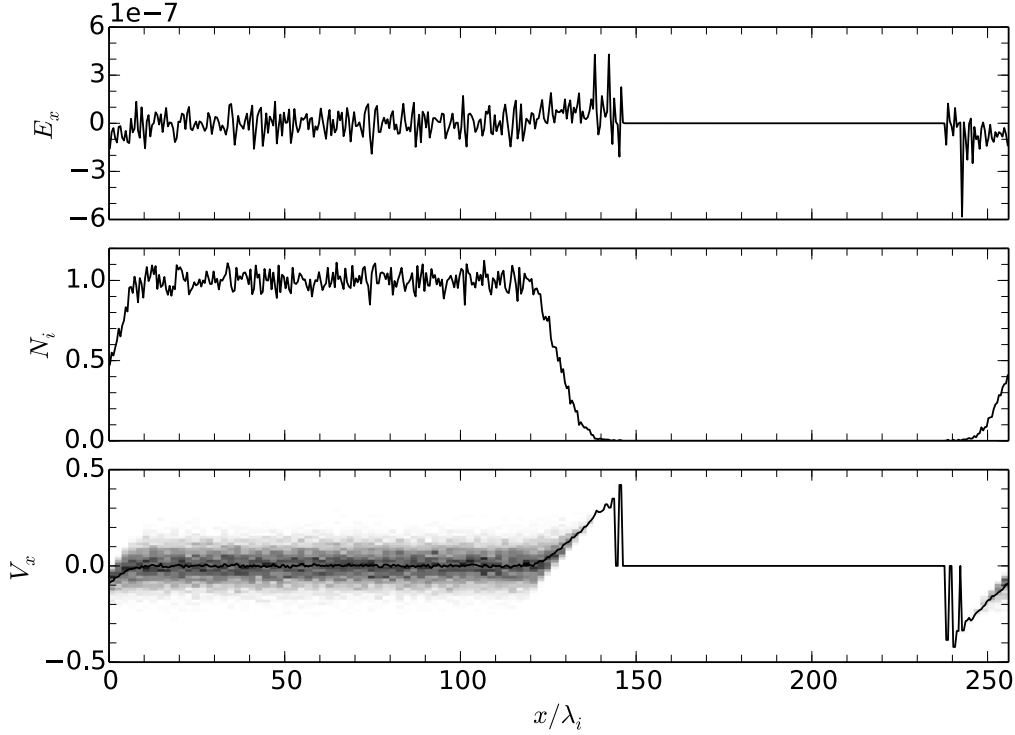


Figure 7: Snapshot of plasma expansion to vacuum at  $\Omega_{ci}t = 48.0$ . The longitudinal electric field (top), density (middle), ion phase space diagram (gray scale) and  $x$  component of the bulk velocity  $V_x$  (bottom) are shown. In a pure vacuum region where ion density is exactly zero, the bulk velocity is also set to zero.

Finally, we note that although the current method introduces finite electron inertia, its application to problems where electron scale physics plays a role must be done with care, because the assumption of a fluid electron is not always appropriate for phenomena with scale length on the order of the electron inertia length encountered in space and astrophysical plasmas, unless electrons are sufficiently cold.

### Acknowledgement

T. A. thanks M. Hoshino, and T. Terasawa for useful discussion. This work was supported by JSPS Grant-in-Aid for Young Scientists (B) 25800101.

### Appendix A. Alternative Derivation of Equation (14)

By taking temporal derivative of Ampere's law and using Faraday's law, we obtain the following equation:

$$-c^2 \nabla \times \nabla \times \mathbf{E} = 4\pi \frac{\partial}{\partial t} \mathbf{J}. \quad (\text{A.1})$$

The total current density is defined as

$$\mathbf{J} = \sum_s q_s \int \mathbf{v} f_s(\mathbf{v}) d\mathbf{v}, \quad (\text{A.2})$$

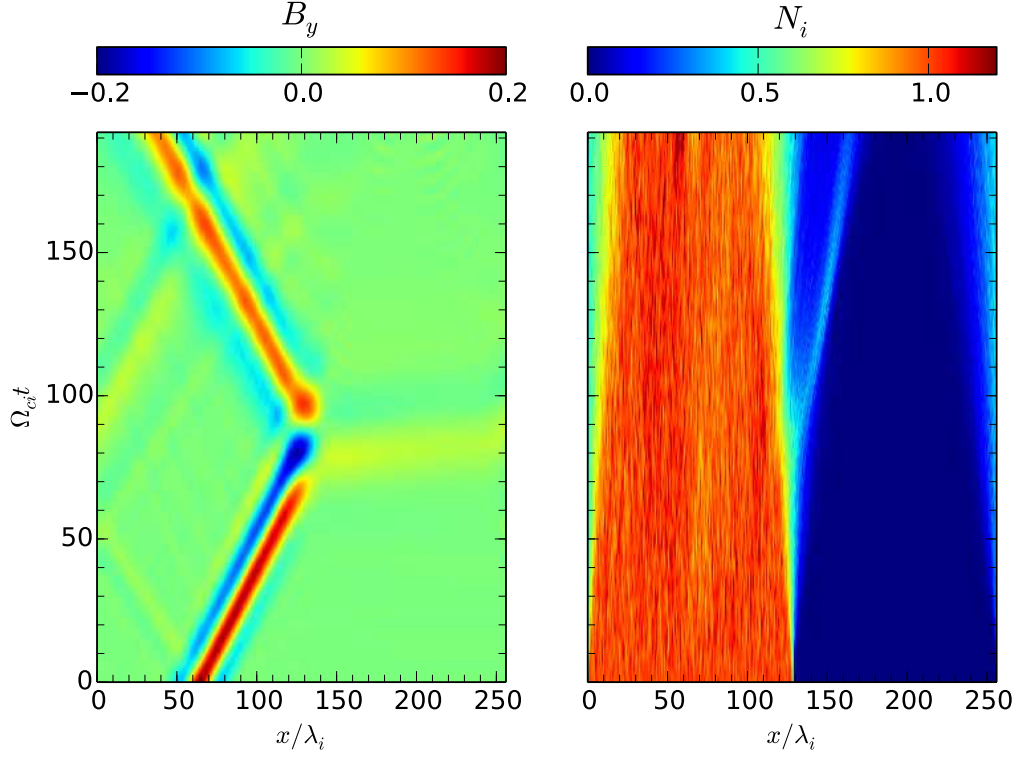


Figure 8: Time evolution of plasma expansion to vacuum with localized wave packet. The transverse magnetic field  $B_y$  (left) and density (right) are shown.

where  $q_s$ ,  $f_s(\mathbf{v})$  is charge and distribution function of particle species  $s$ , and the sum is taken over all particle species. Now we assume that the charged particles are collisionless and traveling under the action of electromagnetic fields. Then, the distribution function  $f_s$  obeys the Vlasov equation

$$\frac{\partial}{\partial t} f_s + \mathbf{v} \cdot \frac{\partial}{\partial \mathbf{x}} f_s + \mathbf{a}_s \cdot \frac{\partial}{\partial \mathbf{v}} f_s = 0, \quad (\text{A.3})$$

where the acceleration is given by the Lorentz force

$$\mathbf{a}_s = \frac{q_s}{m_s} \left( \mathbf{E} + \frac{\mathbf{v}}{c} \times \mathbf{B} \right). \quad (\text{A.4})$$

One may now rewrite the right-hand side of Eq. (A.1) as

$$\begin{aligned} 4\pi \frac{\partial}{\partial t} \mathbf{J} &= \sum_s 4\pi q_s \int \mathbf{v} \frac{\partial}{\partial t} f_s d\mathbf{v} \\ &= - \sum_s 4\pi q_s \int \mathbf{v} \left[ \mathbf{v} \cdot \frac{\partial}{\partial \mathbf{x}} f_s + \mathbf{a}_s \cdot \frac{\partial}{\partial \mathbf{v}} f_s \right] d\mathbf{v} \\ &= - \sum_s \left[ \nabla \cdot \left( 4\pi q_s \int \mathbf{v} \mathbf{v} f_s d\mathbf{v} \right) - 4\pi q_s \int \mathbf{a}_s f_s d\mathbf{v} \right] \\ &= \sum_s \left[ \Lambda_s \mathbf{E} + \frac{\mathbf{\Gamma}_s}{c} \times \mathbf{B} - \nabla \cdot \mathbf{\Pi}_s \right], \end{aligned} \quad (\text{A.5})$$



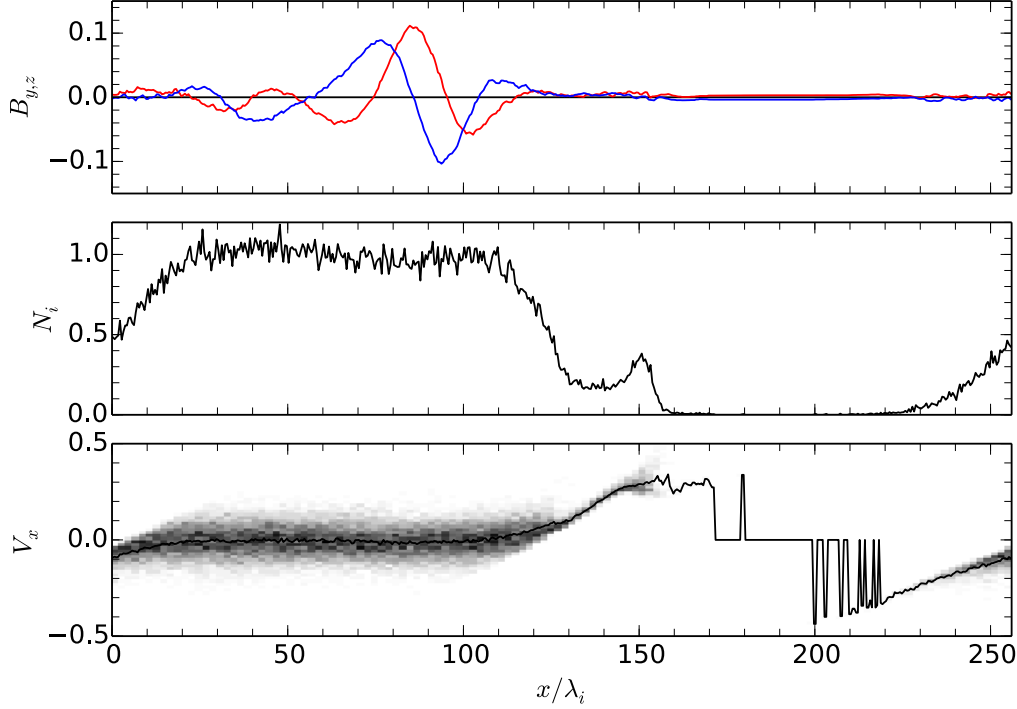


Figure 9: Snapshot of plasma expansion to vacuum with localized wave packet at  $\Omega_{ci}t = 140.0$ . The transverse magnetic field  $B_y$  (red),  $B_z$  (blue) is shown in the top panel, whereas density and ion phase space diagram and bulk velocity  $V_x$  are shown in the middle and bottom panels, respectively.

where  $\Lambda_s$ ,  $\Gamma_s$ ,  $\Pi_s$  are defined by moments of the distribution function

$$\Lambda_s \equiv \frac{4\pi q_s^2}{m_s} \int f_s d\mathbf{v} \quad (\text{A.6})$$

$$\Gamma_s \equiv \frac{4\pi q_s^2}{m_s} \int \mathbf{v} f_s d\mathbf{v} \quad (\text{A.7})$$

$$\Pi_s \equiv 4\pi q_s \int \mathbf{v} \mathbf{v} f_s d\mathbf{v}. \quad (\text{A.8})$$

Note that, in the above derivation, we made use of the fact that  $\nabla_{\mathbf{v}} \cdot \mathbf{a}_s = 0$  for the Lorentz force, and assumed that the distribution function is a rapidly decaying function of velocity: i.e.,  $f_s \rightarrow 0$  for  $\mathbf{v} \rightarrow \pm\infty$ , but otherwise everything is exact.

It is easy to see that  $\Lambda_s$  and  $\Gamma_s$  is inversely proportional to the mass  $\propto 1/m_s$ , and the dominant contribution comes from electrons. The tensor  $\Pi_s$  may be rewritten as

$$\Pi_s = 4\pi q_s \left( n_s \mathbf{V}_s \mathbf{V}_s + \frac{1}{m_s} \mathbf{P}_s \right), \quad (\text{A.9})$$

where  $\mathbf{V}_s$  and  $\mathbf{P}_s$  are the bulk velocity and pressure tensor, respectively. Therefore, the contribution of the pressure gradient is greater from electrons than ions, unless the ion-to-electron temperature ratio is unusually high. The contribution of the term proportional to  $\mathbf{V}_s \mathbf{V}_s$  is usually small, but for electrons, it may not always be ignored because the electron bulk velocity can become as high as the electron Alfvén speed.

Consequently, for typical problems to which the hybrid simulation is applied, it is sufficient to take into account

the electron contribution  $\Lambda_e, \Gamma_e, \Pi_e$  to Eq. (A.1). Then we arrive at

$$\frac{1}{4\pi} (\omega_{pe}^2 + c^2 \nabla \times \nabla \times) \mathbf{E} = \frac{e}{m_e} \left( \frac{\mathbf{J}_e}{c} \times \mathbf{B} - \nabla \cdot \mathbf{P}_e \right) + \nabla \cdot (\mathbf{V}_e \mathbf{J}_e). \quad (\text{A.10})$$

If we further assume the charge neutrality condition  $n_i \approx n_e$ , we have  $\nabla \cdot \mathbf{E} \approx 0$ , and  $\nabla \cdot \mathbf{V}_e \approx 0$ , and Eq. (14) results. Note that the latter condition comes from the fact that temporal and spatial derivatives of the electron density are small on the electron scale,  $\partial n_e / \partial t \approx \partial n_e / \partial x \approx 0$ .

## Appendix B. Validity Range of Variable Mass Ratio

In the present paper, we have introduced a technique to reduce the maximum phase velocity of the system by locally and temporarily reducing the ion-to-electron mass ratio. We think this is not likely to affect the simulation results as far as the ion dynamics is concerned as explained below.

In the linear approximation for a homogeneous plasma, it is possible to estimate the range in which finite electron inertia does not change the ion dynamics. For this, we consider whistler waves propagating parallel to the ambient magnetic field as it gives the maximum frequency in the system which is the most sensitive mode to the electron dynamics. The dispersion relation for parallel propagating right-handed circularly polarized electromagnetic waves in a cold electron-ion plasma is given by

$$1 + \left( \frac{\omega_{pi}}{kc} \right)^2 \frac{\omega}{\omega + \Omega_{ci}} + \left( \frac{\omega_{pe}}{kc} \right)^2 \frac{\omega}{\omega - \Omega_{ce}} = 0 \quad (\text{B.1})$$

where  $\omega/kc \ll 1$  is assumed and the cyclotron frequency  $\Omega_{cs}$  ( $s = i, e$ ) is defined as an absolute value. For  $m_e/m_i \ll 1$ , it may be approximated as

$$\frac{\omega^2}{(\omega + \Omega_{ci})\Omega_{ci}} \simeq \left( 1 - \frac{m_e}{m_i} \frac{\omega}{\Omega_{ci}} \right) \left( \frac{kc}{\omega_{pi}} \right)^2 \quad (\text{B.2})$$

In the limit of  $m_e \rightarrow 0$ , this reduces to the usual whistler mode branch. Assuming that the finite electron inertia becomes important at high frequency regime ( $\omega \propto k^2$ ), a critical wavenumber  $k_c$  beyond which the electron inertia introduces  $O(\Omega_{ci})$  correction to the frequency may be estimated as  $k_c c / \omega_{pi} \simeq (m_i/m_e)^{1/4}$ . The critical wavenumber depends only weakly on mass ratio, implying that the actual value of mass ratio is not important as far as  $m_e/m_i \ll 1$ . In other words, if one wants to model a specific phenomenon correctly up to  $k < k_{max}$ , the range of mass ratio required for this may be determined as  $m_i/m_e \gtrsim (k_{max} c / \omega_{pi})^4$ . The dynamics of ions will not be affected by the artificial modification of the wave dispersion as far as this condition is satisfied.

Similar analysis for the case with nonlinear and/or inhomogeneous effects is not easy in general, but the above condition can be used as a rough measure. Another thing that we do not taken into account in the above analysis is ion kinetic effect such as cyclotron resonance. Concerning the whistler mode, this is justified unless the ion thermal velocity is much larger than the Alfvén velocity, since otherwise the ions cannot resonantly interact with such high frequency waves. For a very high beta plasma such that the ion plasma beta is comparable or larger than the mass ratio ( $\beta \gtrsim m_i/m_e$ ), the ion cyclotron damping may not be negligible even for the whistler branch. Nevertheless, since the general trend is to reduce the real frequency so that the electron inertia becomes less important, one can expect that the above conclusion will roughly hold.

## References

- Birch, P. C., & Chapman, S. C. (2001). Detailed structure and dynamics in particle-in-cell simulations of the lunar wake. *Physics of Plasmas*, 8, 4551–4559.
- Dyadechkin, S., Kallio, E., & Jarvinen, R. (2013). A new 3-D spherical hybrid model for solar wind interaction studies. *Journal of Geophysical Research (Space Physics)*, 118, 5157–5168.
- Farrell, W. M., Kaiser, M. L., Steinberg, J. T., & Bale, S. D. (1998). A simple simulation of a plasma void: Applications to Wind observations of the lunar wake. *Journal of Geophysical Research*, 103, 23653–23660.
- Goldstein, M. L. (1978). An instability of finite amplitude circularly polarized Alfvén waves. *The Astrophysical Journal*, 219, 700–704.

- Harned, D. S. (1982). Quasineutral hybrid simulation of macroscopic plasma phenomena. *Journal of Computational Physics*, 47, 452–462.
- Hesse, M., & Winske, D. (1994). Hybrid simulations of collisionless reconnection in current sheets. *Journal of Geophysical Research*, 99, 11177–11192.
- Hewett, D. W. (1980). A global method of solving the electron-field equations in a zero-inertia-electron-hybrid plasma simulation code. *Journal of Computational Physics*, 38, 378–395.
- Higashimori, K., & Hoshino, M. (2012). The relation between ion temperature anisotropy and formation of slow shocks in collisionless magnetic reconnection. *Journal of Geophysical Research (Space Physics)*, 117, 1220.
- Holmström, M. (2013). Handling Vacuum Regions in a Hybrid Plasma Solver. In N. V. Pogorelov, E. Audit, & G. P. Zank (Eds.), *Numerical Modeling of Space Plasma Flows (ASTRONUM2012)* (p. 202). volume 474 of *Astronomical Society of the Pacific Conference Series*.
- Holmström, M., Fatemi, S., Futaana, Y., & Nilsson, H. (2012). The interaction between the Moon and the solar wind. *Earth, Planets, and Space*, 64, 237–245.
- Horowitz, E. J., Shumaker, D. E., & Anderson, D. V. (1989). QN3D: A Three-Dimensional Quasi-neutral Hybrid Particle-in-Cell Code with Applications to the Tilt Mode Instability in Field Reserved Configurations. *Journal of Computational Physics*, 84, 279–310.
- Kallio, E., & Janhunen, P. (2003). Modelling the solar wind interaction with Mercury by a quasi-neutral hybrid model. *Annales Geophysicae*, 21, 2133–2145.
- Kuznetsova, M. M., Hesse, M., & Winske, D. (1998). Kinetic quasi-viscous and bulk flow inertia effects in collisionless magnetotail reconnection. *Journal of Geophysical Research*, 103, 199–214.
- Leroy, M. M., Winske, D., Goodrich, C. C., Wu, C. S., & Papadopoulos, K. (1982). The structure of perpendicular bow shocks. *Journal of Geophysical Research*, 87, 5081–5094.
- Lipatov, A. S. (2002). *The hybrid multiscale simulation technology: an introduction with application to astrophysical and laboratory plasmas*.
- Nakamura, M. S., Fujimoto, M., & Maezawa, K. (1998). Ion dynamics and resultant velocity space distributions in the course of magnetotail reconnection. *Journal of Geophysical Research*, 103, 4531–4546.
- Nakamura, T. K. M., Fujimoto, M., & Otto, A. (2008). Structure of an MHD-scale Kelvin-Helmholtz vortex: Two-dimensional two-fluid simulations including finite electron inertial effects. *Journal of Geophysical Research (Space Physics)*, 113, 9204.
- Shay, M. A., Drake, J. F., Denton, R. E., & Biskamp, D. (1998). Structure of the dissipation region during collisionless magnetic reconnection. *Journal of Geophysical Research*, 103, 9165–9176.
- Terada, N., Machida, S., & Shinagawa, H. (2002). Global hybrid simulation of the Kelvin-Helmholtz instability at the Venus ionopause. *Journal of Geophysical Research (Space Physics)*, 107, 1471.
- Terasawa, T., Hoshino, M., Sakai, J.-I., & Hada, T. (1986). Decay instability of finite-amplitude circularly polarized Alfvén waves - A numerical simulation of stimulated Brillouin scattering. *Journal of Geophysical Research*, 91, 4171–4187.
- Trávníček, P., Hellinger, P., & Schriver, D. (2007). Structure of Mercury's magnetosphere for different pressure of the solar wind: Three dimensional hybrid simulations. *Geophysical Research Letters*, 34, 5104.
- Winske, D., & Leroy, M. M. (1984). Diffuse ions produced by electromagnetic ion beam instabilities. *Journal of Geophysical Research*, 89, 2673–2688.
- Winske, D., Yin, L., Omid, N., & Karimabadi, H. (2001). Hybrid codes: Past, present and future. In J. Büchner, C. T. Dum, & M. Scholer (Eds.), *Space Plasma Simulation* (p. 62).
- Wong, H. K., & Goldstein, M. L. (1986). Parametric instabilities of the circularly polarized Alfvén waves including dispersion. *Journal of Geophysical Research*, 91, 5617–5628.